Are Direct Current Chromium Deposits Nanogranular?

Craig V. Bishop, Dr. Allen R. Jones, Dr. Agnes Rousseau, Atotech World Wide R&D,
Atotech USA; Dr. Charles McFarland

Crystalline chromium from a variety of electrolytes, deposited using direct current conditions, were examined for grain size, grain uniformity, crystallographic texture, macro /micro stress, impurities and reduced modulus (E_r) using focused ion beam (FIB), scanning transmission electron microscopy (STEM), X-ray diffraction (XRD), electron energy loss spectrometry (EELS), particle induced x-ray emission (PIXE), elastic recoil determination (ERD) and nanoindentation (NI). The resulting data is useful in determining whether a deposit meets the various criteria of being nanogranular.

For more information contact:
Craig V. Bishop
Atotech Worldwide R&D
1750 Overview Drive
Rock Hill, SC 29730 USA
Phone: 803-817-3568
cbishop@atousa.com

Introduction

There are many factors that influence the properties of an electrodeposited material. The factors may include the composition of the electrodeposit, phases which are present, the overall morphology of the electrodeposit, the presence of heterogeneities either deliberately or inadvertently added or an unavoidable constituent of the deposit, the crystallography of the deposit, and the grain size and orientation of the deposit. In fact, it is likely that many of the above factors are linked together to provide commercially acceptable electrodeposits (Benaben[1]).

In recent years considerable attention has been given to materials referred to as nanomaterials, that is materials which are built of submicron scale components including grains, and several papers and books have been written on various aspects of the subject from an electrodeposition standpoint[2,3,4,5,6]. The interest in nanomaterials is not merely a demonstration of creating small objects. Rather, it is a desire to produce materials with otherwise unusual properties. For example, in typical microscale materials decreasing grain size results in an increase in hardness, and a well-known equation, referred to as the Hall-Petch relationship, describes this behavior. However, the Hall-Petch relationship has grain size within the denominator of a fraction and consequently, there is a limit at which diminishing grain size results in hardening, otherwise materials of near infinite hardness would be obtainable. In fact, there is a 'reverse' Hall-Petch region where diminishing grain size results in softer materials. Schietz and Jacobsen[4] simulated this with nanograin copper and found that the maximum predicted strength for nanograin copper occurs at the 15 nm grain diameter regime. In deformation of microscale materials several observations can be made related to plasticity. One of these is that the x-ray diffraction pattern of plastically deformed microscale materials shows a permanent change, peak broadening, associated with stress remaining within the material. This permanent change indicates that the next time the material is subjected to stress there are preexisting stress regions that will hasten material failure. Budrovic, et al.[5] demonstrated that nanogranular electrodeposited nickel does not remain in a peak broadened state with critical grain size in the 20-40 nm range. In more recent developments Lu et al.[6] have demonstrated that nanograined copper at the 100 nm scale, if twinned, will both improve the strength of electrodeposited copper compared to micrograined copper and preserve the conductivity of micrograined copper, unlike 15 nm non grained nanograin copper deposits where conductivity is deleteriously effected, presumably by the large intergranular to granular volume ratio.

From the preceeding it is apparent that nanograined materials offer a very exciting field for materials and electrodeposition to evolve within, and that the exact definition of what is a nanograin may depend as much upon the desired alteration of properties from the microscale as well as size.

How are nanograined electrodeposits created? The classical method is to use a pulse waveform that allows current densities an order of magnitude or more greater than typical DC current densities to be achieved for short periods of time, on the order of 0.02 seconds. During the off phase of the pulse, the locally depleted metal ions are replenished by diffusion and during the next deposition pulse renucleation occurs. This cycle repeats itself so that grain growth is interrupted and restarted producing nanogranular materials. The method to form high volumes of twins is not well understood and may be related to lower deposition temperature and possibly greater direct current equivalent efficiencies[6].

However, pulse plating rectifiers remain rather expensive and implementation of pulse plating at large production scale is a costly retrofit to existing direct current facilities. Is it possible to reap nanocrystalline advantages from direct current deposits? There is some evidence that a few direct current processes produce grain patterns which are quite small[8,9,13]. These deposits tend to come from low efficiency processes where it is feasible that hydrogen production could physically interrupt the deposition process and necessitate renucleation. Has nanocrystallinity been with us in the electroplating community prior to the introduction of pulse rectification?

The fact is that many commercial electrodeposited materials have smaller grains than pyrometallurgically derived equivalents. It is also a fact that the material properties of electrodeposited metals and alloys can significantly differ from pyrometallurgically derived materials. Electrodeposited chromium is an example. The hardness and wear resistance of electrodeposited chromium is significantly greater than pyrometallurgical chromium[7]. Durut, in his dissertation[8], determined that chromium with domain sizes as small as 22 nm can be achieved with direct current and hexavalent electrolyte.

Our recent research has concentrated on the study of functional chromium nucleation[9], heterogeneities, corrosion, and stress[10], and grain/domain size, which will be reported in this paper using the results of recent, focused ion beam (FIB), x-ray diffraction (XRD) domain size, nanoindentation (NI) and atomic force microscopy (AFM) studies. Because composition is a consideration with all materials particle induced x-ray emission (PIXE) and elastic recoil detection (ERD) for hydrogen presence were also used to baseline elemental compositions.

Various methods may be employed to determine grain or continuously diffracting domain size. These include transmission electron microscopy (TEM), scanning TEM (STEM), high contrast back scatter scanning electron microscopy (HCBS-SEM), and ion beam induced secondary electron detection (IBI-SED) using an FIB where grain size may be determined rather unequivocally, various high energy diffraction methods including XRD where the continuously diffracting domain (CDD) size is determined, and surface analyses using scanning probes such as an AFM.

TEM and STEM are very attractive but sample preparation is critical and tedious. For TEM thin slices of material are observed using an electron beam that passes through the sample and various observational methods can be employed including bright field illumination, convergent beam electron diffraction (CBED), and selected area diffraction (SAD). Historically, electroplated samples examined by TEM are prepared so that the material parallel to the surface was thinned for TEM and the width of the grains could be estimated. However, this means of sample preparation ignores the important length measurement of grains that would require thin slices from the cross section of the material.

The electron backscatter methods can be successfully employed to measure grain size if the samples are highly polished either in plan or cross section. But, there are resolution limitations that make use of this method very difficult if grains have a dimension less than a micron.

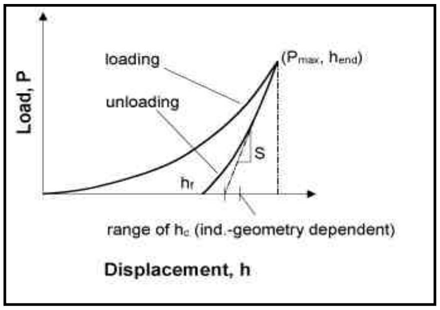

Figure 1 Experimental determination of Er is based upon careful measurement of load and displacement using a very small indenter.

FIB can facilitate grain measurement in two ways. Cross sectional lamellae can be prepared from the material which can then be used for STEM, TEM and associated chemical analyses such as electron energy loss spectroscopy (EELS) and x-ray fluorescence (XRF). This method requires that the lamellae be removed using a micromanipulator either in-situ or ex-situ. The FIB may also be used to obtain images of a highly polished cross sectional surface produced by using the ion beam to create a 'trench' in the surface and induce secondary electrons with the ion beam. These ion beam induced secondary electron images have contrasts that are sensitive to the orientation of crystalline surfaces from which they are emitted.

XRD is a simpler experimental method to use but does not measure grain size as unequivocally as do the preceding techniques and interpretation must be used to infer the size of diffracting regions. The principle concept is that peak broadening occurs as domain sizes decrease. These domain sizes are an approximation of the perpendicular-to-the-surface length of the average crystallite. However, peak broadening as well as peak shifts can be affected by deposit stress as well as domain size. When residual stress and preferred orientations are present compensation for peak broadening due to stress and domain size becomes complicated. Residual stress data on the experimental samples can be obtained using by XRD using the Reuss method with the assumption that electrodeposited materials are transversely isotropic, that is the stress from any point in the sample is equivalent in directions parallel to the surface but zero in the perpendicular to substrate direction.[13,14,15,16,17,*]

In the sample, we can write:

$$\left\langle \sigma_{ij}^{S} \right\rangle_{\mathrm{Reuss}} = \begin{bmatrix} \sigma_{\mathrm{Reuss}} & 0 & 0 \\ 0 & \sigma_{\mathrm{Reuss}} & 0 \\ 0 & 0 & 0 \end{bmatrix}$$

We measure:

$$\varepsilon_{33}^{L} = S'^{L}_{33ij}\sigma^{L}_{ij} = S'^{L}_{33kl}\, a^{S}_{ki}\, a^{S}_{lj}\, \sigma^{S}_{ij} = S'^{L}_{33ij}\left(a^{S}_{i1}\, a^{S}_{j1} + a^{S}_{i2}\, a^{S}_{j2}\right)\sigma_{\mathrm{Reuss}}$$

With:

$$S'^{L}_{33ij} = S'^{c}_{2}\,\delta_{ij} + \frac{1}{2} S'^{c}_{4}\,\delta_{3i}\delta_{3j} + S^{c}_{0}\left(a^{S}_{3k}\right)^{2} a^{S}_{ik}\, a^{S}_{jk} \quad \text{and} \quad S^{C}_{0} = S'^{C}_{1} - S'^{C}_{2} - \frac{1}{2} S'^{C}_{4}$$

Where σ: stress; ε: strain; S: elastic compliance tensor of the crystallite; L: Laboratory reference (L_1, L_2, L_3); S (subscript): sample reference; C: crystal reference a^{S}_{ij} : Direction cosines in the rotation matrix from the sample (S) reference to the laboratory (L) reference: δ: Kroniker delta.

---

[*] *Additional information on our method to determine residual within highly textured electrodeposits may be obtained from Agnes Rousseau, agnes.rousseau@atousa.com*

	Temp oC	*[SO4]*	*Current Density A/dm2*	*Sample*	*Mrb Density Mrb/cm*	*Std. Dev. Mrb/cm*
Conv.	*55*	*2.5*	*15*	*M1*	*250*	*55*
				M2	*220*	*89*
				M3		
			30	*M4*	*120*	*35*
				M5	*110*	*37*
				M6		
	70			*P6HotA*	*0*	
Etch-free	*60*	*3.2*	*30*	*M7*	*1600*	*206*
				M8	*1600*	*263*
				M9		
			60	*M10*	*1500*	*278*
				M11	*1500*	*165*
				M12		
			75	*M13*	*1600*	*236*
				M14	*1500*	*135*
				M15		
Etch-free	*65*	*3.2*	*30*	*M16*	*1200*	*116*
				M17	*1100*	*105*
				M18		
			60	*M19*	*970*	*310*
				M20	*1000*	*122*
				M21		
			75	*M22*	*1000*	*135*
				M23	*940*	*136*

Table 1 Experimental samples used in this study.

In order to accurately calculate the stress of the deposit Young's modulus and Poissons ratio of the material need to be included in the calculation. Electrodeposits are difficult to use for classical measurement of these two important material properties and a new method[11] employing nanoindentation combined with AFM is useful. AFM is also useful in measuring surface features and if the forces experienced by the tip vary as the tip passes over intergranular regions grain dimensions may be estimated with either plan or cross sections. In addition to measuring surface features atomic force microscopes may be equipped with nano indentation devices. The nanoindentation instrument obtains data related to the modulus (E) and Poisson's ratio (υ) as reduced modulus (E_r) often represented as:

$$1/E_r=(1-\nu_i^2)/E_i-(1-\nu_s^2)/E_s$$

where the subscripts describe the indenting (i) and sample material (s) and results are experimentally determined as illustrated in figure 1 from the stiffness of the material obtained by unloading during indentation.

$$S=2(A)^{0.5}/(\chi)^{0.5}E_r$$

Results of the nanoindentation reduced modulus study are reported in this conferences companion paper[10] and AFM data on surface irregularity is used in this study.

Experimental:

Functional chromium from hexavalent electrolyte was deposited onto ½" hexagonal steel or brass rods obtained from McMaster-Carr that were subsequently polished to a 600 grit surface on two non adjacent sides to ensure relatively smooth substrate.

The matrix for the deposition used three types of electrodeposited chromium obtained from conventional, fluoride[*] (mixed-catalyst), and high-efficiency etch-free[**] baths. All of the baths contain sulfate (SO_4^{2-}) and chromium (VI) oxide (Cr_2O_3). The sulfate and fluoride

---

[*] *HCR 840 Chromium Plating Process, Atotech*

[**] *HEEF 25 Chromium Plating Process, Atotech*

compounds act as catalysts. The high-efficiency etch-free bath contains a non-halide catalyst. Chromium cannot be electrodeposited from an aqueous chromic acid solution unless one or more catalysts are present. Depending on which catalysts are present and the plating parameters, between 10 and 30% of the cathodic current will be used to reduce hexavalent chromium (Cr^{6+}) to chromium metal. Also, depending upon the electrolyte, deposition temperature and current density, heterogeneities known as micro cracks and micro ribbons will be present in varying amounts[10]. Table 1 summarizes the deposits used in this study.

X-ray diffraction (XRD) was performed using a four-axis (1/4 circle Eulerian cradle) Bruker D8 Discover instrument utilizing $Cu_{k\alpha}$ radiation and a NaI scintillation detector. The sample is irradiated and diffraction peaks measured using powder geometry and peak intensities that are greater than expected based upon randomly oriented reference materials are due to grains that are preferentially orientated with one crystallographic plane parallel to the substrate. The presence of preferred orientation, or texture, is generally associated with electrodeposited chromium and the presence of preferred orientation complicates the analysis of electrodeposited chromium. Confirmation of preferred orientation as well as measurement of the peaks at non-basal-plane angles is important. Our assumption is that the XRD patterns obtained from electrodeposited chromium are fiber textured and determination of preferred orientation as well as analysis of peaks at interplanar angles that are out of the basal laboratory reference plane can be simply performed by moving the hexagonal rod to appropriate chi (χ) angles at constant phi (φ) angle perpendicular to the circle of the detector and x-ray source.

As the broadening of X-ray diffraction peaks is due to three factors: instrumental effects, "crystallite size" or CDD, and lattice strain; in our work we needed to separate the different effects by following different procedures, the classic Scherer method, and a Lorentzian peak broadening method which takes into account broadening due to stress[18]. In all cases integral breadth peak widths were used instead of FWHM. All experimental peak broadening was corrected from the instrumental effects using the diffraction pattern of a sample heat treated at 500 ºC for 8 hours. A Gaussian profile was then used to subtract the instrumental broadening from the observed broadening. Next, we considered that the two other effects (CDD and strain) lead to Lorentzian broadenings. The corrected broadening is simply equal to the sum of these two broadenings as follows:

1. Broadening of x-ray diffraction peaks due to small domain size only is obtained from the Scherrer formula:

$$B_{CDD} = \frac{k\lambda}{L\cos\theta}$$

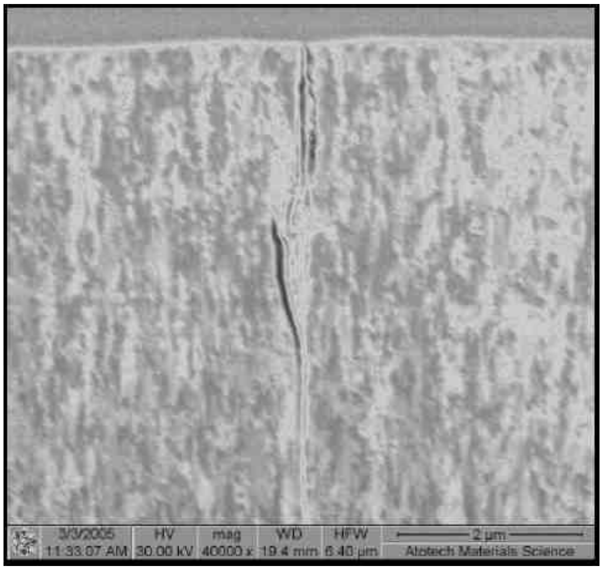

Figure 2 Ion beam induced secondary electron image of etch free chromium in cross section.

λ is the wavelength (1.54056 Å);
θ is the Bragg angle;
L is the "average" crystallite size measured in a direction perpendicular to the surface of the specimen;
And κ is a constant (cubic crystals k = 0.94).

2. Taking into account broadening due to strain:

$$B_{strain} = 4\eta\tan\theta$$

η is the lattice strain in the material. This effect (microscopic range) is different from the macroscopic effect due to residual stress that leads to peak displacement. It represents the deviation of the material crystallites from the perfect crystal.

3. Therefore the total broadening, B_r, of the diffraction peak is finally equal to:

$$\Rightarrow \boxed{B_r = \frac{k\lambda}{L\cos\theta} + 4\eta\tan\theta \Leftrightarrow B_r\cos\theta = \frac{k\lambda}{L} + 4\eta\sin\theta}$$

And, we can plot $B_r\cos\theta$ against $\sin\theta$ and should obtain a straight line with 4η as the slope and $\kappa\lambda/L$ as the intercept

The FIB is an FEI Nova 200 Ga ion beam instrument equipped with Pt gaseous ion source (GIS) a selective carbon mill (SCM) and an Ascend Instruments micromanipulator. This instrument is multi beam with capability of the primary ion beam and a field emission electron beam simultaneously converging at nanometer resolution.

The NI and AFM that were used in this study consist of a Hysitron Triboscope Nanomechanical Test Instrument interfaced to a Digital Instruments (Veeco Metrology Group) Dimension 3100 atomic force microscope (AFM). A Berkovich diamond indenter (three-sided pyramidal tip, total angle included 142.3^{o} deg, average radius of curvature 100 nm) was used. The instrument load frame compliance and indenter tip area function were calibrated with a vendor-supplied fused silica specimen assuming a contact depth independent elastic modulus. The calibration load range was 1000-8000 µN, with a maximum indenter contact depth of about 120 nm. The tip area function was a best fit to a reduced modulus of 69.6 GPa for the fused silica. Indentations on specimens were usually carried out at loads chosen to produce contact depths of about 100 nm. Six to nine indents were performed on each sample. The Oliver/Pharr analysis procedure was followed to extract values of the indentation modulus and the hardness from the experimental load versus displacement curves. Coating surface profiles were examined in the contact AFM mode with the Berkovich indenter tip.

RESULTS:

At the time of preparation for this paper TEM and STEM studies of chromium samples have not been completed. Sample preparation using FIB has convergence problems associated with maintaining environmental temperature stability, compensation for magnetic substrates, and the antiferromagnetic chromium coating.

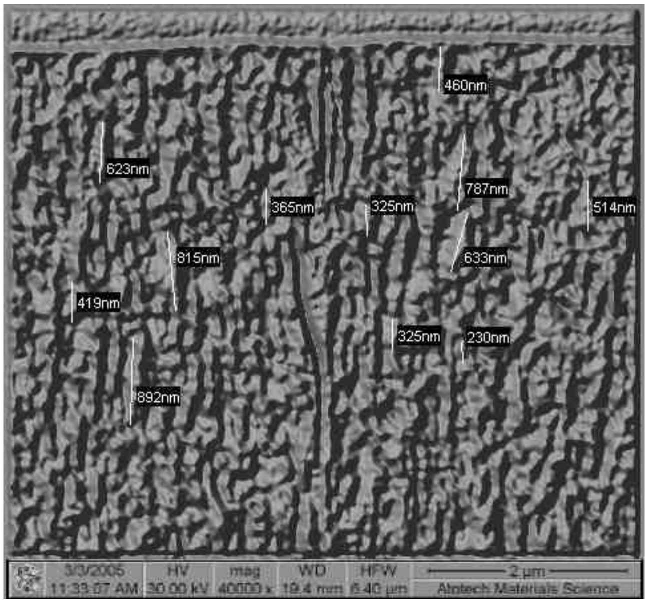

Figure 3 Image enhanced ion beam induced secondary electron image of etch free chromium in cross section.

High resolution IBI SED from the FIB also suffers from the combination of magnetic substrates and the antiferromagnetic chromium coating however some imaging has been completed. In figure 2 a low-resolution image of an etch free (222) preferred orientation chromium deposit has contrast corresponding to different orientations of grains within the deposit. Figure 3 is the same image, subjected to texturization image enhancement[12] and from which the length of apparent grains was measured resulting in an average length of 534 nm with a standard deviation of 216 nm.

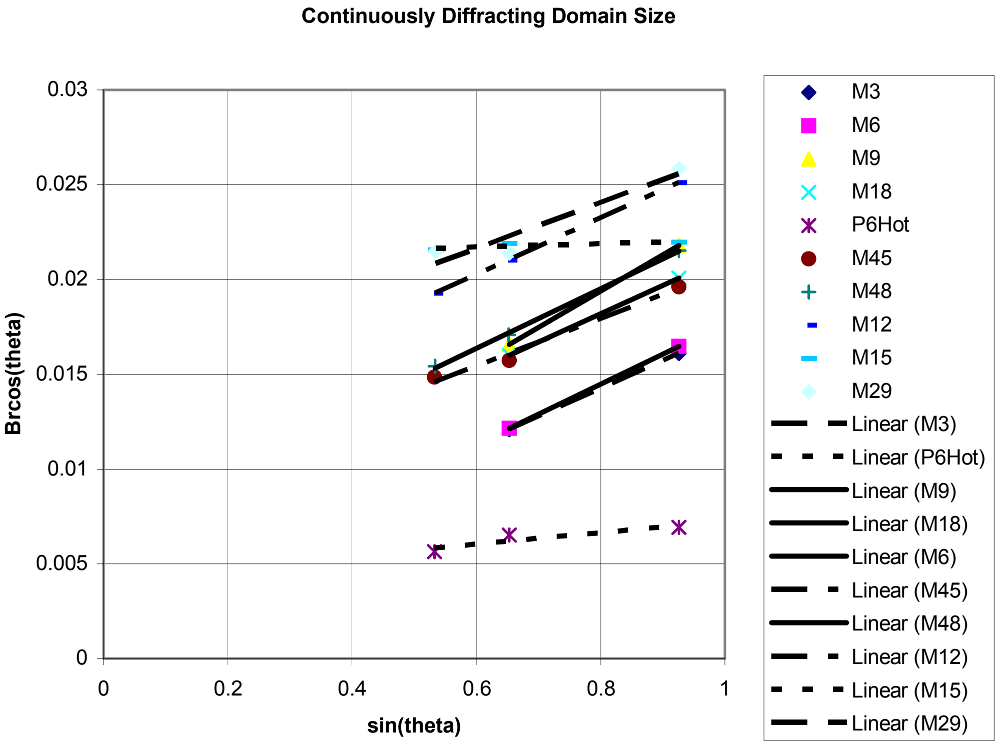

Figure 4 Plotted data using modified Scherrer equations from various functional chrome deposits illustrating the range of intercept values is rather small.

Table 2: Continuously Diffracting Domain size using the Scherrer formula with and without correction for strain induced microdeformation.

Sample	Scherrer method (nm)	CDD + microdeformations	
		CDD (nm)	Strain (x10-3)GPa
M3*	10	60	3.7
M6*	10	80	4.0
M9*	10	35	4.8
M12	6	15	3.7
M15	7	7	0.2
M18*	9	25	3.8
M21*	9	20	3.6
P6HotA	20	35	0.8

**: only 2 peaks availables.*

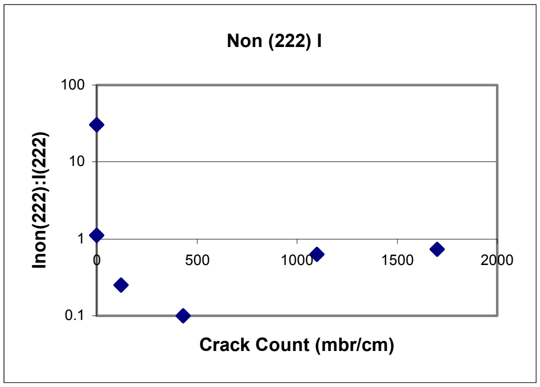

Figure 5 Intensity of non (222) peaks vs. crack count of various chrome deposits.

The XRD studies encounter a problem with chromium electrodeposits related to the strong (222) preferred orientation. The use of peaks at small diffraction angles is the best means to separate the effects of stress and CDD and having as many peaks as possible to plot the slope of the equation is also desirable. Yet, due to preferred orientation, for some samples, without changing chi angles, only 2 peaks could be used at 81.5° (211) and 135.6° (222). At best three peaks were used at 64.4° (200), 81.5° and 135.6°. Therefore the measured CDD should be interpreted with extreme caution although all data appears to converge at similar CDD scales equating to the 10-80 nm range (figure 4).

The CDD obtained by considering only the broadening due to the crystallite size (Scherrer) as well as those obtained using compensation of broadening due to stress are shown in table 2. The contribution to broadening due to stress-induced microdeformations is evident in estimating the CDD.

In figure five the relative intensities (χ=0) of non (222) peaks to the preferred orientation (222) peak were plotted as a function of crack count from table 1. Additional plots in figures six and seven attempt to correlate the CDD size with crack count and the intensity of non (222) reflections. From this data it appears as if the presence of non (222) peaks is related to increased crack count when crack count exceeds 200-300 mbr/cm.

AFM images of the surface may be used to obtain statistical information on the distribution of particles or grains. A representative AFM is presented in figure eight. The AFM data suggests that surface features have average diameters of 220 nm and range from 100 nm to

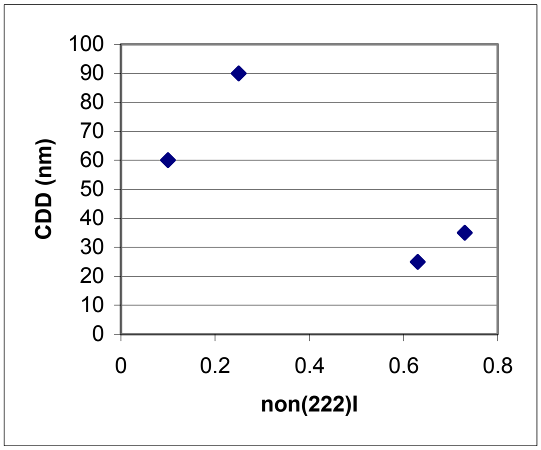

Figure 6 CDD size as a function of non (222) relative intensity.

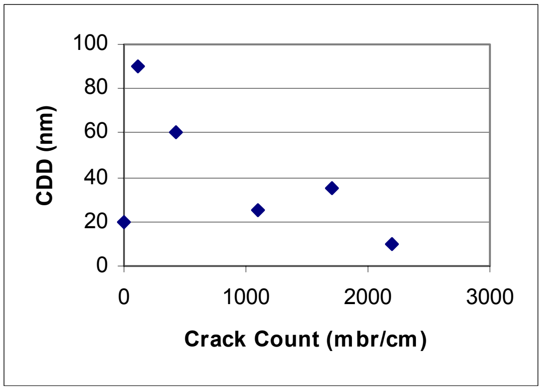

Figure 7 Variation of measured CDD size with crack count.

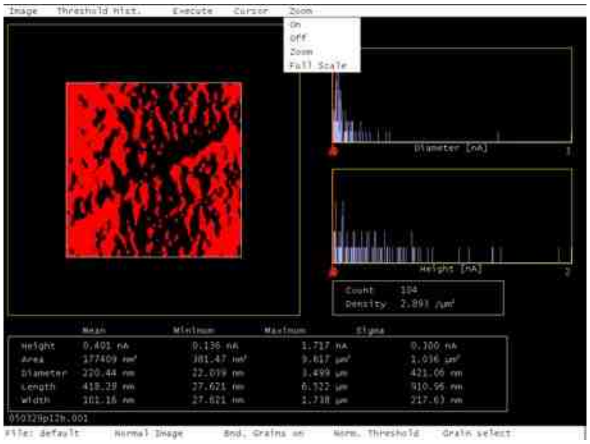

Count 104
Density 2.893 /µm²

	Mean	Minimum	Maximum	Sigma
Height	0.401 nA	0.136 nA	1.717 nA	0.300 nA
Area	177409 nm²	381.47 nm²	9.617 µm²	1.036 µm²
Diameter	220.44 nm	22.039 nm	3.499 µm	421.06 nm
Length	418.29 nm	27.621 nm	6.522 µm	910.96 nm
Width	101.16 nm	27.621 nm	1.738 µm	217.63 nm

Figure 8 AFM image, in the nano amp mode, used to determine the scale of surface irregularities.

400 nm with a histogram skewed towards lower values.

PIXE of chromium deposits revealed that sulfur and oxygen are present in the deposit as well as chromium. ERD revealed that hydrogen is present and that its concentration becomes less when the samples are annealed.

Discussion and Conclusions:

Previous studies dealing with chrome nucleation[9] demonstrated that nucleating functional chromium material has length scale dimensions in the 20 to 100 nm range directly measured by high-resolution field emission SEM.

In this study on bulk functional chromium we have obtained contradictory evidence of grain size using three methods. FIB data suggests grain sizes on the scale of 500 nm with grains that are roughly elongated and tiled rather than strictly columnar. AFM data of surface irregularities suggests scales of 200 nm. The continuously diffracting domain size, determined by XRD, is in the 30 nm scale.

The heterogeneity (microribbons), present in electrodeposited functional chromium seems linked to changes in both preferred orientation of the deposit and changes in observed CDD which may suggest that there are two domains of materials with different nano crystalline size regimes, the bulk material and material within the ribbon regions. This observation supports recent data that suggests [10] micro ribbons are comprised of chromium of different orientation than the bulk electrodeposit and likely are smaller grained than bulk grains.

Durut suggested that chromium grains might be comprised of multiple domains of nearly identical orientation in all directions, more closely packed together than typical grains that would have significant intergranular spacing and whose rotational orientations would be distinctly different.

From the preceding the question of the precise nature of commercial electrodeposited chromium grain size must await the results of FIB prepared STEM and TEM cross sectional studies. The data from the STEM and TEM studies can then be compared to CDD data obtained by XRD at different chi angles.

References.

1. J. Torres-Gonzalez and P. Benaben, Metal Finishing, June, 2003, p 107-116.
2. G. Palumbo, et al., Plating and surface Finishing, Feb. 2003, p 36-45
3. Gary Hodes (Editor), *Electrochemistry of Nanomaterials*, Wiley-VCH Verlag GmbH, Weinheim, D., 2002.
4. Jakob Schiøtz and Karsten W. Jacobsen, *Science* 5 September 2003; 301: 1357-1359
5. Z. Budrovic, H. Van Swygenhoven, P. M. Derlet, S. Van Petegem, B. Schmitt, *Science*, Vol 304, Issue 5668, 273-276, 9 April 2004
6. Lei Lu, Yongfeng Shen, Xianhua Chen, Lihua Qian, and K. Lu, *Science* 16 April 2004; 304: 422-426
7. Y. Kobayashi, J. I. Nagasawa, K. Watanabe, K. Nakamura, T. Sasaki, and Y. Hirose, 3rd *International Conference on Chromium*, St. Etienne, FR, April, 2001.
8. Frederic Durut, April 7, 1999 Doctoral Dissertation, Soutenue a Saint-Etienne.
9. Craig Bishop, Allen Jones, Chris Ringholz, *International Conference on Chromium*, St. Etienne, FR, June, 2004
10. Allen Jones and Craig Bishop, SurFin 2005, AESF, St. Louis, MO, June, 2005.
11. W. C. Oliver and G. M. Pharr, J. Mater. Res., **7**, No. 6, June 1992, pp. 1564-1583.
12. Corel® PhotoPaint 11, version 11.633, © 2002 Corel Corporation.
13. B.M. Clemens and J.A. Bain, “Stress Determination in Textured Thin Films Using X-Ray Diffraction”, MRS Bulletin, 1992, 46-51
14. M. Zaouali, J.L. Lebrun and P. Gergaud, “X-ray diffraction determination of texture and internal stresses in magnetron PVD molbdenum thin films”, Surface and Coatings Technology, 50 (1992), 5-10
15. M. Leoni, U. Welzel, P. Lamparter, E.J. Mittemeijer and J.-D. Kamminga, “Diffraction analysis of internal strain-stress fields in textured, transversely isotropic thin films: theoritical basis and simulation”, Philosophical Magazine A, 2001, vol. 81, No. 3, 597-623
16. V. Hauk, “Structural and Residual Stress Analysis by Nondestructive Methods”, Elsevier, 1997
17. I.C. Noyan and J.B. Cohen, “Residual Stress: Measurement by Diffraction and Interpretation”, Springer-Verlag, 1987
18. C. Suryanarayana and M. Grant Norton, “X-Ray Diffraction: A practical Approach”, Plenum Press, 1998